PHYSICSAccess Research Paper
ISSN Online: 2756-3898, ISSN Print: 2714-500X https://doi.org/10.47514/phyaccess.2026.6.2.004

First-Principles Investigation of Alkaline-Earth Metal Co-Doped Hexagonal WO_3 for Enhanced Near-Infrared Optical Response

Umar Ibrahim[1], Alhassan Shuaibu[2], Adamu Muhammed[2], Yakubu T Aliyu[2], Musa Lawal[1], and Timothy Bulus[3]

[1]Department of Science Laboratory Technology, Federal Polytechnic Kaura Namoda, Zamfara State, Nigeria
[2]Department of Physics, Faculty of Physical Science, Kaduna State University, Kaduna, Kaduna State, Nigeria
[3]Department of Science Education/Physics Unit, Faculty of Education, Kaduna State University, Kaduna, Kaduna State, Nigeria

Corresponding E-mail: ibrahimumar.physics@gmail.com

Received 09-03-2026
Accepted for publication 20-06-2026
Published 10-07-2026

Abstract

The structural, thermodynamic, electronic, and optoelectronic properties of co-doped hexagonal tungsten trioxide (h-WO_3) are investigated using Density Functional Theory (DFT) with the HSE06 hybrid functional and Density Functional Perturbation Theory (DFPT). To enhance near-infrared (NIR) response, beryllium is paired with alkaline-earth metals (Mg, Ca, Sr, and Ba) to form co-doped hexagonal tungsten bronze-like (h-HTB) configurations. Phonon-dispersion calculations confirm the dynamical stability of the co-doped systems, while formation-energy analysis indicates that the (Be, Ba) configuration is the most thermodynamically favorable, with a minimum formation energy of -2.68 eV. Electronic-structure calculations show that co-doping introduces impurity states within the pristine 3.3 eV band gap, leading to substantial band-gap narrowing across the dopant series. In particular, the (Be, Ba) system exhibits a reduced band gap of 0.9 eV, which is favorable for NIR absorption. Dielectric-function analysis further reveals a crossover in the real part of the dielectric function, $\varepsilon_1(\omega)$, together with a resonant feature in the imaginary part, $\varepsilon_2(\omega)$, near 0.9 eV, suggesting possible plasmonic behavior in the low-energy region. The calculated optical absorption spectra show strong NIR absorption with coefficients exceeding 10^4 cm^{-1} and trends comparable to those of $Cs_{0.33}WO_3$ benchmark systems, while retaining visible-light transparency. Overall, the results identify (Be, Ba) co-doped h-WO_3 as a thermodynamically favorable and optically promising candidate for smart-window and photothermal applications.

Keywords: h-WO_3; Alkaline Earth Metals (AEM); HSE06 hybrid functional; optical absorption spectra; near-infrared region (NIR).

I. Introduction

Energy-efficient smart windows and photothermal technologies require materials with strong and tunable light-absorption characteristics, particularly in the visible and near-infrared (NIR) spectral regions, where a substantial fraction of solar energy is concentrated [1–5]. Among the materials explored for such applications, transition metal oxides (TMOs) have garnered considerable attention due to their versatile optical, electronic, thermal, and electrochemical properties [6–8]. Within this class, tungsten trioxide (WO_3) and its derivatives have emerged as especially promising candidates owing to their tunable optical absorption, pronounced electrochromic behavior, robust thermal stability, and relatively low-cost fabrication [9-10]. These characteristics enable WO_3-based systems to modulate solar radiation and heat transmission while maintaining chemical durability, making them attractive for smart-window and photothermal applications.

Despite these advantages, several challenges limit the widespread application of specific WO_3 polymorphs, particularly hexagonal tungsten trioxide (h-WO_3), in smart windows, sensors, batteries, and optoelectronic devices. One major limitation is the intrinsic metastability of the hexagonal phase, which is thermodynamically less favorable than the monoclinic ground state at room temperature [11]. In addition, h-WO_3 undergoes significant structural distortion during guest-ion intercalation and deintercalation, which can lead to lattice deformation and long-term cycling degradation [12]. The physical properties of h-WO_3 are also highly sensitive to non-stoichiometry and defect states. Although oxygen vacancies strongly influence its electronic structure, carrier concentration, and optical response [13], uncontrolled defect generation can introduce disordered trapping states. Furthermore, h-WO_3 exhibits a moderate-to-wide indirect band gap of approximately 2.5–3.0 eV, which limits efficient solar harvesting in the visible and NIR regions [14]. This limitation is compounded by its relatively low intrinsic electrical conductivity, which adversely affects charge-transport kinetics and electrochromic switching speed [15].

Nevertheless, the open tunnel-like framework of h-WO_3 provides a favorable structural platform for property modification. These limitations can, in principle, be mitigated through nano-structuring and low-dimensional design, lattice-strain engineering, defect engineering with controlled nonstoichiometry, and substitutional doping via mono-doping or co-doping strategies. Because strong optical absorption and effective modulation in the NIR region are essential for energy-saving smart windows and solar-thermal evaporators, tailoring the optoelectronic properties of h-WO_3 toward enhanced NIR activity remains an important research direction [16].

In this context, the design of non-stoichiometric tungsten bronzes (M_xWO_3, where M denotes an alkali, alkaline-earth, or transition-metal ion) and sub-stoichiometric oxides (WO_{3-x}) has emerged as an effective route for tuning the properties of WO_3-based materials. Experimental and optical studies of tungsten bronzes have shown that heavy ion insertion or controlled oxygen deficiency can inject a large number of free electrons into the W 5d conduction band states. The resulting increase in carrier density may induce strong NIR optical response and possible plasmonic behavior, transforming the material from an insulating state into a highly conducting oxide [17].

More broadly, studies on plasmonic TMOs have demonstrated that collective electronic oscillations can be leveraged to achieve strong and selective light absorption without significantly compromising visible transparency. However, optimizing the balance among NIR absorption, structural stability, and lattice strain requires predictive atomic-scale insight into the relationship between dopant chemistry, defect formation, and electronic structure. This challenge has motivated extensive theoretical investigations based on Density Functional Theory (DFT) [18]. Standard local and semilocal exchange-correlation approximations, such as LDA and GGA-PBE, often underestimate the band gap of TMOs and do not adequately localize the d-electrons associated with oxygen vacancies or dopant states, which can lead to inaccurate metallic descriptions.

Recent DFT studies employing more advanced electronic-structure methods, particularly the screened Heyd–Scuseria–Ernzerhof (HSE06) hybrid functional, have substantially improved the description of these systems by reducing self-interaction errors and providing more reliable band-edge positions, localized defect states, and optical absorption spectra in doped transition metal oxides [19]. Such approaches are especially valuable for tracking how metal dopants modify the electronic structure and extend optical absorption into the NIR region.

Motivated by these considerations, the present study systematically investigates the structural, thermodynamic, electronic, and optoelectronic properties of single- and co-doped h-WO_3 systems. A first-principles framework based on the HSE06 hybrid functional [20] is employed to achieve an accurate treatment of exchange-correlation effects, while density functional perturbation theory (DFPT) is used to evaluate lattice dynamics and vibrational stability. By examining the interplay among dopant coordination, electronic structure, and dielectric response, the study aims to provide atomistic insight into the design of NIR-active h-WO_3 architectures with improved optoelectronic performance for next-generation smart-window and photothermal applications.

II. Computational Details

Density functional theory (DFT) calculations were carried out using the Quantum ESPRESSO package together with the thermo_pw interface [21]. Exchange–correlation effects were initially treated within the generalized gradient approximation (GGA) using the Perdew–Burke–Ernzerhof (PBE) functional [22], in combination with projector augmented-wave (PAW)

pseudopotentials [23]. A converged plane-wave energy cutoff of approximately 680 eV was employed for both pristine and doped systems. Structural relaxations were performed using a 12 × 12 × 1 Monkhorst–Pack k-point mesh [24]. For each configuration, the lattice parameters and cell volume were first optimized, after which the atomic positions were relaxed until the force on each atom was less than 0.01 eV Å^{-1}. All subsequent electronic and optical properties of pristine h-WO_3 and the doped hexagonal tungsten bronze (HTB) systems were evaluated using the optimized structures.

To construct the doped models, one W atom in the hexagonal cell was replaced by a Be atom for the single-doped systems. For the co-doped systems, a neighboring W site was additionally replaced by an alkaline-earth metal (AEM = Mg, Ca, Sr, or Ba). The single-doped configurations therefore correspond to $A_{0.02}W_{0.98}O_3$ (A = Be, Mg, Ca, Sr, and Ba), while the co-doped systems correspond to $Be_{0.02}A_{0.02}W_{0.96}O_3$ (A = Mg, Ca, Sr, and Ba). Owing to computational limitations, the calculations were restricted to low dopant concentrations, which remain below those typically reported for experimentally synthesized tungsten bronzes, $AxWO_3$ ($0.15 \leq x \leq 0.30$) [25].

Electronic-structure calculations were performed using the Heyd–Scuseria–Ernzerhof (HSE06) range-separated hybrid functional [26]. HSE06 improves the description of electronic structure in transition-metal oxides by partially replacing semilocal exchange with short-range exact exchange, thereby reducing self-interaction errors and improving band-gap predictions [27]. In this formalism, the Coulomb potential is separated into short-range and long-range components using a screening parameter of μ = 0.2 Å^{-1} [28]. The short-range exchange contains 25% Hartree–Fock exchange mixed with 75% PBE exchange, while the long-range exchange is described by the PBE functional. For Brillouin-zone integration in the hybrid-functional calculations, a reduced 6 × 6 × 1 k-point mesh was used for the band-structure calculations. Density-of-states (DOS) calculations were performed using a denser k-point sampling containing at least 125 k-points to ensure convergence.

A. Phonon Dispersion Calculation

Phonon dispersions were calculated using density functional perturbation theory (DFPT) as implemented in the thermo_pw driver within the Quantum ESPRESSO environment. A 4 × 4 × 4 q-point Monkhorst–Pack grid was used to sample the Brillouin zone. The non-analytical contribution to the dynamical matrix in the q → 0 limit was included to account for longitudinal optical–transverse optical (LO–TO) splitting. Owing to the large mass differences among the dopant species, high-frequency optical modes above 800 cm^{-1} were also examined as localized vibrational signatures of the dopant environment.

B . Formation Energy Calculation.

The stability of the doped structures was assessed using the formation energy, defined as in (1) [29].

$$E_{for} = E_{tot}(doped) - E_{tot}(pristine - WO_3) - \mu_{dopant} \quad (1)$$

Where $E_{tot}(doped)$ is the total energy for the doped supercell containing one or two AEM atoms, $E_{tot}(pristine - WO_3)$ is the total energy of the pure supercell and μ_{dopant} is the chemical potential of the dopant species. A negative formation energy indicates that the doped configuration is energetically favorable relative to the chosen reference states.

C. Optical Properties Calculation

The optical absorption spectra were calculated from the complex dielectric functions $\varepsilon(\omega)=\varepsilon_1(\omega) + i\varepsilon_2(\omega)$. The imaginary part $\varepsilon_2(\omega)$ is obtained from the momentum matrix elements between the occupied and the empty electronic states, and the real part $\varepsilon_1(\omega)$ is obtained from $\varepsilon_2(\omega)$ by means of the Kramer–Kronig relation [30-31]. The Drude term, playing an important role in the energy region below ~1 *eV*, is also included in the theoretical curves [30].

$$\varepsilon_2(\omega) = \frac{2\pi e^2}{\Omega\varepsilon_0}\sum_{k,v,c}\left|\vec{\lambda}.\langle\psi_k^c|u.r|\psi_k^v\rangle\right|^2\delta(E_k^c - E_k^v - E) \quad (2)$$

Here, the integral is over the Brillouin zone, $u, \omega, e, \psi_k^c, \psi_k^v$ are the polarization vector of the incident electric field, the frequency of light, the electronic charge, and the conduction and valence band wave function at k, respectively.

$$\varepsilon_1(\omega) = 1 + \frac{2}{\pi}\mathrm{P}\int_0^\infty \frac{\omega'\varepsilon_2(\omega')}{\omega'^2-\omega^2}d\omega' \quad (3)$$

Where P denotes the integral's principal value. In this work, $\varepsilon_1(\omega)$ and $\varepsilon_2(\omega)$ were averaged over three polarization vectors (*x*, *y*, and *z*) to take the tensor nature of the dielectric into account.

The knowledge of the real and imaginary dielectric functions' expression was computed to obtain the optical absorption spectrum $\alpha(\omega)$. Hence, the optical absorption spectra of pure and co-doped h-WO_3 were calculated using (4), as implemented in the thermo_pw interface of Quantum ESPRESSO.

$$\alpha(\omega) = \sqrt{2}\omega\left[\sqrt{\varepsilon_1^2(\omega) + \varepsilon_2^2(\omega)} - \varepsilon_1(\omega)\right]^2 \quad (4)$$

III. Results and Discussion

A. Structural properties

The optimized structure of a 2 × 2 × 1 supercell of h-WO_3 is shown in Fig. 1. All intercalated metal atoms were incorporated in the plane of apical oxygen atoms.

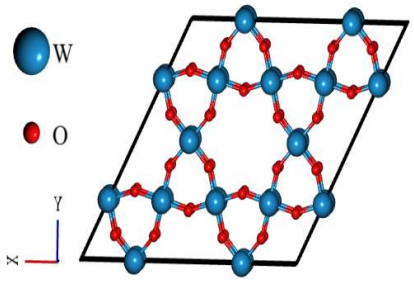

Fig. 1. Optimized structure of 2 × 2 × 1 supercell of h-WO_3.

Fully optimized lattice parameters of pure h-WO_3 and HTBs in comparison with the experimental values are summarized in Table I. It is found that the lattice parameters of pure h-WO_3 after structural optimization are in good agreement with the previous theoretical [32] and experimental [33] results. These results demonstrate that TC and HC can accommodate any dopant, including AEM. Incorporation of AEM is expected to cause significant changes in lattice constants and other structural properties. Fig. 2 gives the optimized single- and co-doped ($A_{0.02}W_{0.98}O_3$, A = Be, Mg, Ca, Sr, and Ba) and co-doped $Be_{0.02}A_{0.02}W_{0.96}O_3$ (A = Be, Mg, Ca, Sr, and Ba) systems, respectively.

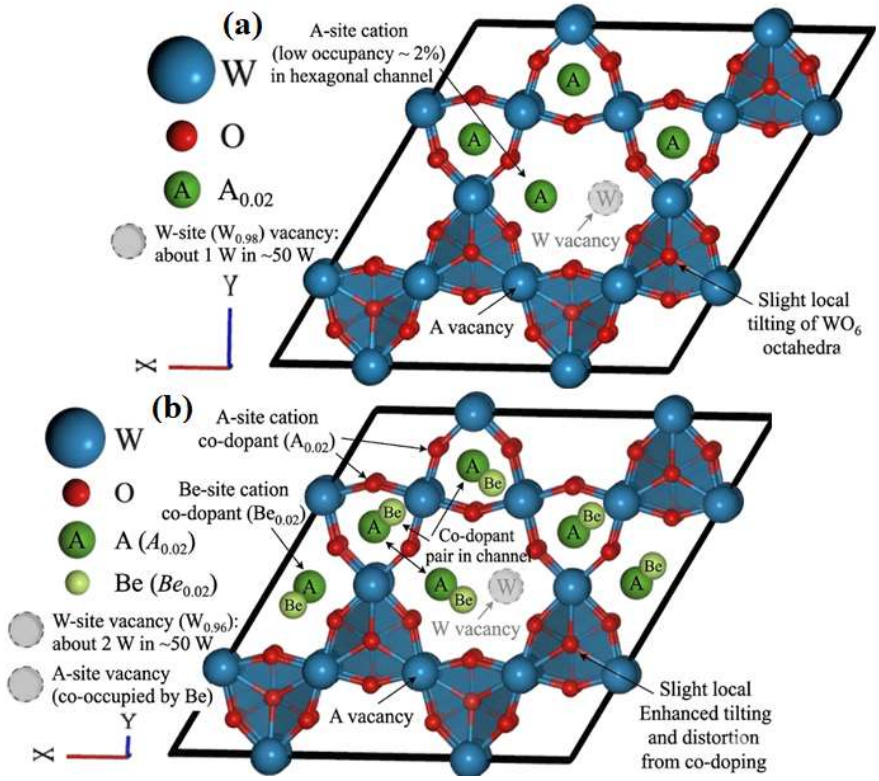

Fig. 2. Optimized structure of (a) $A_{0.02}W_{0.98}O_3$ and (b) $Be_{0.02}A_{0.02}W_{0.96}O_3$, (A= Be, Mg, Ca, Sr, and Ba).

The optimized structure of $A_{0.02}W_{0.98}O_3$, (see Fig. 2 (a)) highlights a robust framework of corner-sharing WO_6 octahedra forming open hexagonal tunnels that host low concentrations of A-site dopants. The incorporation of alkaline earth metals (A = Be, Mg, Ca, Sr, Ba) can be understood considering established tungsten bronze chemistry and defect physics reported in the literature [31]. Consistent with previous studies on hexagonal WO_3, smaller cations such as Be^{2+} and Mg^{2+} exhibit stronger electrostatic interactions with surrounding oxygen atoms, leading to relatively small lattice distortion and better structural stability of the WO_6 network [34]. Their small ionic radii allow them to reside closer to the center of the central W, minimizing octahedral tilting. In contrast, larger cations such as Ca^{2+}, Sr^{2+}, and Ba^{2+} induce noticeable lattice expansion and local distortion, as also observed in related HTB systems where larger alkali or alkaline earth ions increase the c-axis lattice parameter and promote octahedral tilting [35]. This size-dependent distortion aligns with the tolerance factor concept commonly used in perovskite-related structures, where mismatch between ionic radii leads to structural flexibility and tilting of octahedra. Furthermore, the presence of W-site vacancies (~2%) in the structure agrees with defect-mediated stabilization mechanisms widely reported for non-stoichiometric tungsten oxides. Such vacancies act as charge compensators for the incorporation of divalent A-site dopants, leading to the formation of mixed valence states (W^{5+}/W^{6+}), which are known to significantly influence electrical conductivity and optical absorption [36]. Similar findings have been reported in doped WO_3 and tungsten bronze systems, where defect-induced states near the conduction band enhance n-type conductivity and are responsible for electrochromic behavior. Comparatively, studies on alkali-doped WO_3 (e.g., M_xWO_3, where M = Na, K) demonstrate that increasing ionic size enhances metallic-like conductivity due to increased carrier concentration and bandwidth broadening [13]. However, in AEM-doped systems, the divalent nature of dopants introduces a more complex balance between carrier generation and structural distortion. For larger dopants such as Ba, excessive lattice distortion may localize charge carriers,

reducing mobility, an effect also noted in Ba-doped WO_3 films [37].

For the optimized co-doped structure $Be_{0.02}A_{0.02}W_{0.96}O_3$, (see Fig. 2 (b)), the hexagonal tungsten bronze (h-HTB) phase introduces an additional level of structural and electronic complexity compared to single A-site doping. In this configuration, both Be and the alkaline earth cation (A = Mg, Ca, Sr, Ba) occupy the central W, forming co-dopant pairs while maintaining a framework of corner-sharing WO_6 octahedra. The presence of dual dopants, alongside an increased concentration of W-site vacancies (~4%), significantly enhances local lattice distortions, as evidenced by the more pronounced tilting of the WO_6 octahedra and channel asymmetry. From a structural standpoint, the small ionic radius and high charge density of Be^{2+} cause it to occupy off-center positions within the channels, often stabilizing nearby A-site vacancies or forming defect complexes with larger A-site cations. This cooperative interaction resembles defect clustering mechanisms reported in co-doped oxide systems, where smaller cations act as local "anchors" that modulate strain induced by larger dopants [38]. In contrast to single doping, where distortion scales primarily with ionic size, co-doping introduces competing strain fields: Be tends to contract the lattice locally, while larger cations such as Sr^{2+} and Ba^{2+} promote expansion. This interplay leads to enhanced octahedral tilting and local symmetry breaking, consistent with observations in mixed-cation WO_3 and perovskite oxides [39].

Electronically, the increased W-site vacancy concentration plays a crucial role in charge compensation for the dual incorporation of divalent cations. This results in a higher density of reduced tungsten species (W^{5+}), which can introduce localized states within the band gap or near the conduction band minimum. Similar behavior has been reported in defect-rich WO_3 and tungsten bronze systems, where oxygen or cation vacancies enhance n-type conductivity and optical absorption [40]. Importantly, co-doping is known to improve carrier concentration while simultaneously tuning carrier mobility through structural distortion, an effect widely explored in transparent conducting oxides and electrochromic materials [41]. Comparatively, co-doping strategies have been successfully employed in related oxide systems such as TiO_2, ZnO, and perovskite oxides to achieve synergistic improvements in electronic and optical properties. For example, in co-doped TiO_2, the introduction of two different cations creates defect states that enhance visible-light absorption while maintaining structural stability [42]. Similarly, in WO_3, mixed-cation occupancy has been shown to broaden conduction bands and improve electronic transport compared to single-dopant systems [43]. However, excessive distortion, particularly with larger A-site cations like Ba may lead to carrier localization, echoing findings in heavily doped WO_3 films, where structural disorder limits conductivity [44]. Overall, the co-doped $Be_{0.02}A_{0.02}W_{0.96}O_3$ system demonstrates a clear synergistic effect: Be acts to locally stabilize the Structure and modulate defect formation, while the larger A-site dopants tune lattice dimensions and electronic bandwidth. This dual-dopant approach provides a prevailing pathway for engineering the balance between structural distortion, defect chemistry, and electronic performance. Compared to single doping, co-doping offers enhanced flexibility in tailoring material properties, making these systems promising for advanced applications in electrochromic devices, photocatalysis, and energy storage.

B. Phonon Dispersions

To evaluate the structural integrity and dynamical stability of the pristine and doped h-WO_3 systems, their phonon dispersion spectra across the high-symmetry lines of the Brillouin zone were analyzed. In computational materials science, the definitive criterion for dynamic stability is the total absence of imaginary frequencies (vibrations dropping below 0 cm^{-1}), a condition satisfied by all configurations as they exhibit exclusively positive phonon frequencies across the entire Brillouin zone.

The acoustic branches consisting of Longitudinal Acoustic (LA) and Transverse Acoustic (TA) modes govern the elastic stability of the lattice. For the pristine h-WO_3 in Fig. 3(a), single Be-doped in Fig. 3(b), and (Be, Mg)-co-doped configurations in Fig. 3(c), these branches remain steep, smooth, and well-defined, indicating robust restoring forces, strong lattice cohesion, and minimal structural distortion. However, progressing down Group II to the (Be, Ca)-co-doped structure shown in Fig. 3(d) and continuing further down to (Be, Sr) in Fig. 3(e) and (Be, Ba) in Fig. 3(f), a clear trend of declining dynamic stability emerges. Heavier and bulkier dopants introduce severe lattice softening, characterized by the noticeable flattening of LA and TA modes near the zone boundaries, alongside significant LO-TO optical splitting and localized impurity modes. This behavior reveals a clear rise in lattice anharmonicity and severe structural perturbation caused by the massive steric hindrance of the larger cations.

Consequently, based on the comparative analysis of the acoustic and optical phonon profiles, the (Be, Mg)-co-doped h-WO_3 system in Fig. 3(c) is identified as the most dynamically stable configuration among the doped structures. Because the atomic size and mass of Mg are highly compatible with the host matrix, this configuration provides an optimal balance of electronic modification while preserving the cleanest, most rigid lattice integrity with minimal localized strain.

C. Formation Energy

To further investigate the stability of the doped system, the formation energy was computed using (1). The computed formation energies for the doped systems are summarized in Table I.

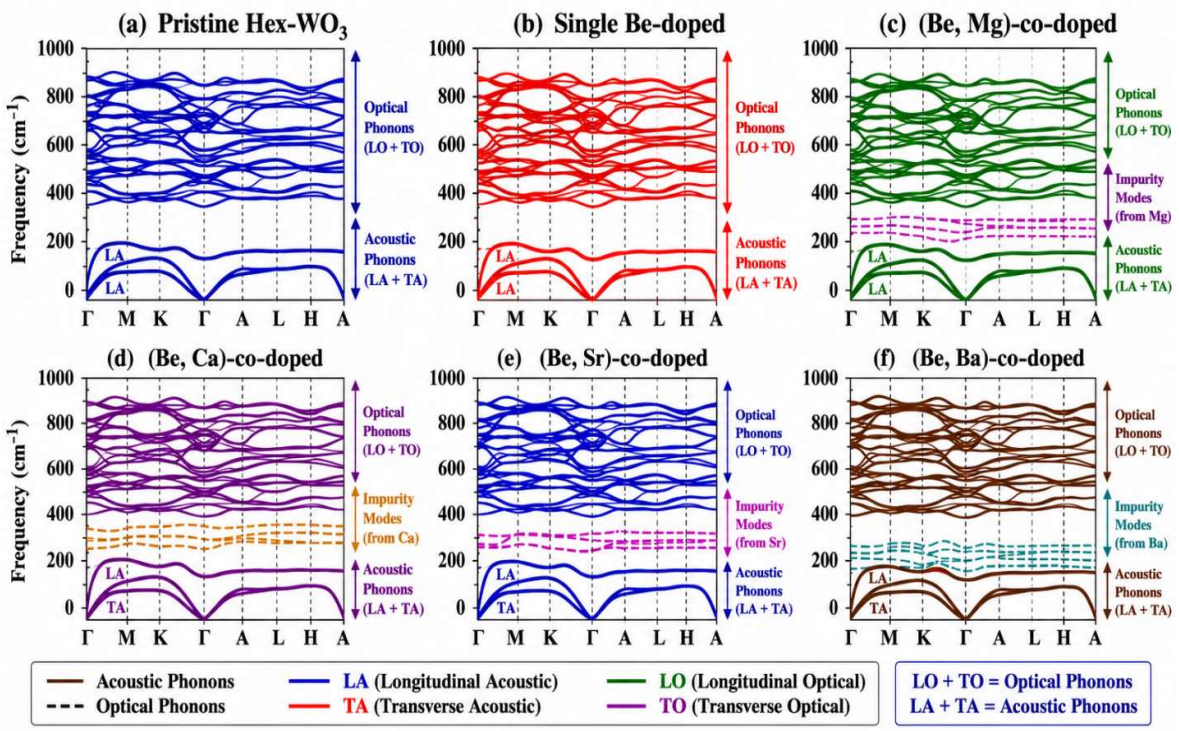

Fig. 3. Phonon dispersions of (a) pristine h-WO_3 and (b) single Be-doped, (c) (Be, Mg)-co-doped, (d) (Be, Ca)-co-doped, (e) (Be, Sr)-co-doped, and (f) (Be, Ba)-co-doped.

Table I: Calculated lattice parameters (a, c), formation energy (E_{for}) of pure h-WO_3 and different hex tungsten bronzes, as compared with other theoretical results and experimental data.

Material	a (Å)	c (Å)	E_{for} (eV)HSE06
Pure	7.298[a]	3.899[a]	-
	7.438[b]	3.827[b]	-
	7.453 (This work)	3.833 (This work)	0
Be-single-doped	7.451	3.833	-1.24
Mg- single-doped	7.453	3.834	-1.85
Ca- single-doped	7.456	3.835	-2.12
Sr- single-doped	7.458	3.836	-1.45
Ba- single-doped	7.463	3.837	-3.973
(Be, Mg)-co-doped	7.508	3.837	-1.98
(Be, Ca)-co-doped	7.500	3.840	-2.35
(Be, Sr)-co-doped	7.497	3.841	-2.48
(Be, Ba)-doped	7.480	3.845	-2.68

[a] see Ref. [32]; [b] see Ref. [33].

From the calculated data presented in Table I, the optimized lattice constants for the pure monolayer were determined to be a = 7.453 Å and c = 3.833 Å. These results exhibit excellent agreement with prior theoretical reports, showing minimal discrepancies against the reference values of a = 7.298 Å and 7.438 Å from previous works, alongside c = 3.899 Å and 3.827 Å. This high degree of precision confirms that the hybrid DFT functional, core pseudopotentials, and plane wave cutoff energies employed herein are fully capable of accurately reproducing the ground-state structural properties of the host matrix, establishing a trustworthy baseline for evaluating subsequent doping and co-doping configurations.

Upon the introduction of single alkaline earth metal dopants (Be, Mg, Ca, Sr, and Ba) into the host framework, a systematic and monotonic expansion of the in-plane lattice parameter a is observed, shifting from 7.451 Å for Be up to 7.463 Å for Ba. This structural evolution correlates precisely with the periodic increase in ionic radii down Group II (Be^{2+}, Mg^{2+}, Ca^{2+}, Sr^{2+}, Ba^{2+}). Incorporating cations with larger atomic volumes into the native lattice site induces localized steric hindrance,

forcing the surrounding atoms to adjust outward to minimize local strain. Concurrently, the out-of-plane lattice parameter c experiences a subtle, highly rigid expansion ranging sequentially from 3.833 Å to 3.837 Å. The highly localized nature of this expansion within the ab-basal plane indicates that single-atom substitution drives an anisotropic structural distortion, preserving the rigid out-of-plane scaffolding while expanding the local coordination pockets.

Interestingly, the co-doped architectures wherein a tiny Be atom is paired with a progressively larger Group II co-dopant reveal a counterintuitive structural interplay along the a-axis. While the (Be, Mg)-co-doped system reaches the maximum in-plane expansion of a = 7.508 Å, further pairing of Be with larger ions (Ca →Sr→ Ba) triggers a steady lattice contraction along the a-axis, dropping down to 7.480 Å for the (Be, Ba) configuration. This anomalous trend is balanced by a significant elongation along the out-of-plane c-axis, which peaks at 3.845 Å in the (Be, Ba) monolayer. This behavior points to an overarching volume-compensation mechanism: the severe geometric mismatch between the exceptionally small Be radius and the bulky Ba radius forces a local tilting or rotation of the coordination polyhedra, compressing the in-plane lattice while expanding along the vertical axis to relieve asymmetric mechanical stress.

To ascertain the experimental feasibility and relative stability of these modified monolayers, the formation energies (E_{for}) were systematically evaluated using the HSE06 functional. All single- and co-doped configurations yielded negative formation energies, confirming that these chemical modifications are globally exothermic and thermodynamically stable. Among the single-doped materials, Ba substitution demonstrates the highest thermodynamic stability with a deeply favorable formation energy of -3.973 eV. Conversely, Be single doping possesses the least negative formation energy, -1.24 eV, owing to the substantial local strain penalty exacted by its small ionic volume. Crucially, the data reveal that co-doping acts as an energetic stabilizer for the less favorable Be species; pairing Be with larger alkaline earth metals drops the formation energies significantly, ranging from -1.98 eV down to -2.68 eV for the (Be, Ba) system. This synergistic stabilization proves that the lattice expansion and chemical pressure supplied by the heavier alkaline earth co-dopants effectively cancel out the severe structural stress induced by Be, rendering these co-doped multi-component 2D monolayers highly viable candidates for experimental synthesis.

To fully understand the structural integrity and experimental feasibility of the doped h-WO_3 systems, their dynamical, structural, and thermodynamic properties must be reconciled. Dynamically, all configurations are stable as they show an absence of imaginary phonon frequencies. However, the phonon spectra reveal that heavier, bulkier dopants like Ca, Sr, and especially Ba induce strong lattice softening and severe structural distortion due to their large ionic radii. On a structural level, this geometric mismatch is confirmed by the lattice parameters: single dopants cause a monotonic expansion, while (Be, X)-co-doped configurations trigger an anisotropic volume-compensation mechanism, compressing the in-plane a-axis and stretching the vertical c-axis to accommodate the massive steric hindrance. Interestingly, while these structural distortions make the heavier dopants appear dynamically less favorable via phonon softening, they are highly favored thermodynamically. The formation energies(E_{for}) are entirely negative, meaning all systems are globally exothermic and chemically stable. Crucially, pairing the exceptionally small Be atom (which suffers a heavy local strain penalty alone at -1.24 eV) with larger alkaline earth metals down the group systematically drops the formation energy down to -2.68 eV for the (Be, Ba) system. Consequently, a clear trade-off emerges, while a lighter co-dopant like Mg preserves the cleanest, most rigid host lattice integrity (optimal dynamic stability), the heavier co-dopants like Ba offer the strongest chemical driving force and energetic stabilization (optimal thermodynamic stability), rendering all these multi-component 2D monolayers highly viable for experimental synthesis. Consequently, a clear trade-off emerges, while a lighter co-dopant like Mg preserves the cleanest, most rigid host lattice integrity (optimal dynamic stability), the heavier co-dopants like Ba offer the strongest chemical driving force and energetic stabilization (optimal thermodynamic stability), rendering all these multi-component 2D monolayers highly viable for experimental synthesis.

D. Electronic Properties.

1) Band structure

The design of hexagonal tungsten trioxide (h-WO_3) for solar energy harvesting necessitates a precise tuning of the electronic band structure to accommodate the near-infrared (NIR) spectrum, which constitutes approximately 53% of total solar irradiance. While pristine h-WO_3 possesses a wide band gap of approximately 3.3 eV (see Fig. 4(a)), limiting its activity to the ultraviolet region, the introduction of alkaline earth metal dopants (Be, Mg, Ca, Sr, Ba) serves as a transformative strategy to narrow this gap through the creation of localized impurity states. Among these, the (Be, Ba) co-doped system (see Fig. 4(f)) emerges as the most promising candidate for high-efficiency NIR harvesting, achieving a calculated band gap as low as 0.9 eV, which aligns perfectly with the standard NIR range of 0.9 eV to 1.65 eV.

The effectiveness of these dopants in narrowing the band gap is largely governed by the atomic radius and the resulting lattice distortion or "chemical pressure" exerted on the h-WO_3 framework. Beryllium (Be) and Magnesium (Mg): These smaller cations tend to introduce mid-gap states that moderately reduce the gap. Single Be-doped systems typically narrow the gap to approximately 2.45 eV (see Fig. 4(b)), while (Be, Mg) co-doping can shift it further toward 1.90 eV (see Fig. 4(c)). These values sit at the edge of the visible and NIR-I boundary, offering decent solar absorption but failing to

capture the deeper NIR-II regions. Calcium (Ca) and Strontium (Sr) are examples of larger cations that can induce more significant structural modifications. Research on Ca-doped metal oxides has shown a reduction in band gap energy from 2.7 eV to approximately 2.2 eV in some configurations [45], though co-doping strategies involving Sr have demonstrated much deeper shifts, at times reaching as low as 0.35 eV to 0.5 eV in highly defective perovskite-like oxides, extending absorption deep into the NIR-II region. Fig. 4(d), (Be, Ca) co-doped further reduced the band gap to 1.45 eV, as well as 1.15 eV in Fig. 4(e), which is still within the NIR-II region. The (Be, Ba) co-doping provides the most balanced electronic profile. This leverages the high electronegativity of Be and the large ionic radius of Ba to compress the forbidden region to 0.9 eV. This specific value is ideal because it maximizes NIR absorption while maintaining a high enough potential for secondary applications like photocatalysis.

The transition from a wide-gap insulator to an NIR-active semiconductor is driven by the emergence of impurity states within the band gap. As the dopant concentration increases, these states broaden into "impurity bands," effectively merging with the valence or conduction bands to create a narrowed gap (E_g). For applications such as smart windows and photothermal conversion, the (Be, Ba) co-doped system is a promising candidate because its 0.9 eV electronic transition energy enables a high infrared blocking capability while potentially maintaining better visible-light transmittance than more metallic tungsten bronzes [46]. In contrast, while Sr-rich phases can achieve even lower gaps (0.35 eV), they often result in a "quasimetallic" behavior that may lead to excessive visible light absorption, which is undesirable for transparency-focused applications [47].

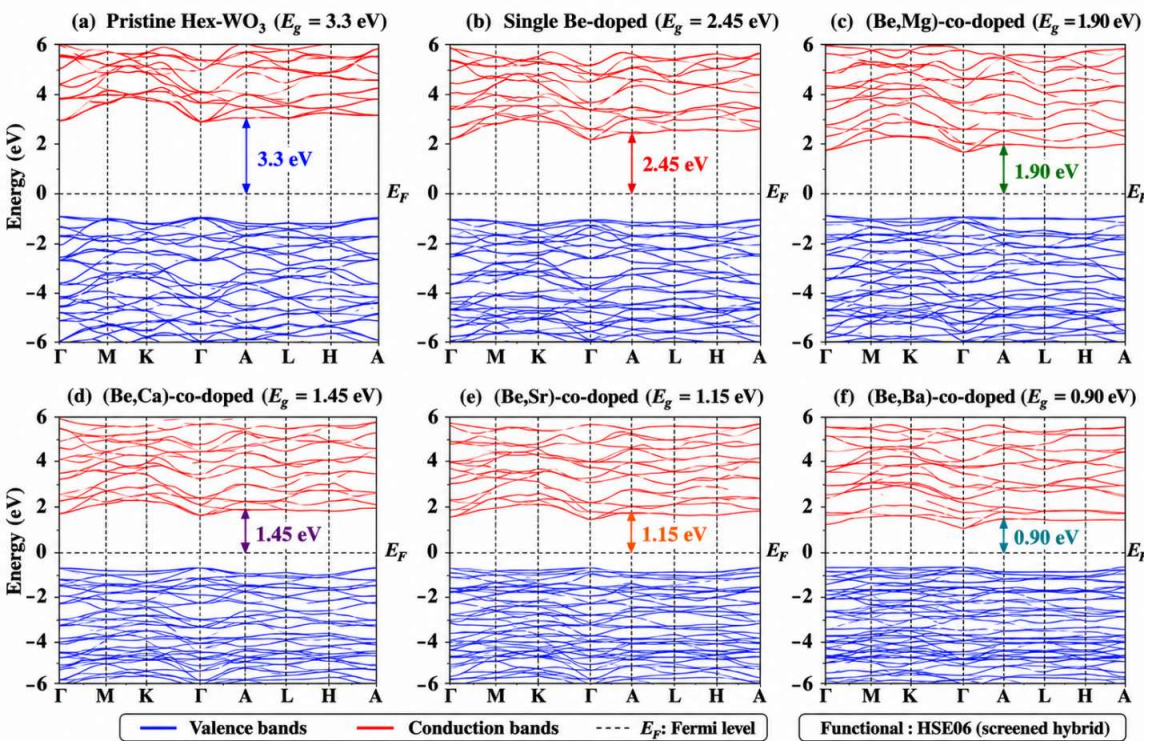

Fig. 4. Calculated band structure of (a) pristine h-WO_3, (b) single Be-doped, (c) (Be, Mg)-co-doped, (d) (Be, Ca)-co-doped, (e) (Be, Sr)-co-doped, and (f) (Be, Ba)-co-doped h-WO_3 systems. Using HSE06 screened hybrid functional.

2) Total Density of State (TDOS) and Projected Density of State (PDOS)

To elucidate the atomistic mechanisms underlying the modulation of the electronic properties of hexagonal tungsten trioxide (h-WO_3) upon mono- and co-doping, the total density of states (TDOS) and partial density of states (PDOS) were systematically analyzed, as depicted in Fig. 5(a–f). For pristine h-WO_3 (see Fig. 5(a)), the calculated band gap (E_g) is 3.30 eV, which is in excellent alignment with the reported experimental result [39], proving the fidelity of the HSE06 hybrid functional framework. The corresponding PDOS reveals that the valence band maximum (VBM) is predominantly governed by the localized O 2p orbitals, whereas the conduction band minimum (CBM) is overwhelmingly composed of empty, delocalized W 5d states.

Upon the introduction of a single Be dopant (see Fig. 5(b)), the fundamental band gap undergoes a significant reduction to 2.45 eV. This band gap narrowing is driven by the emergence of mid-gap impurity states located right above the Fermi level (E_F = 0 eV), which are primarily attributed to the hybridization

between the dopant Be 2s states and the host O 2p orbitals. This trend of progressive band gap narrowing is remarkably pronounced when traversing the alkaline-earth metal co-doped configurations (Be, M, where M = Mg, Ca, Sr, Ba), as illustrated in Fig. 5(c–f). Specifically, the fundamental band gap systematically contracts from 1.90 eV for (Be, Mg)-co-doped h-WO_3 down to an ultra-narrow gap of 0.90 eV for the (Be, Ba)-co-doped architecture. This drastic reduction in band is intimately linked to the increasing atomic radius and changing chemical hardness of the co-dopant species (Mg^{2+}→Ba^{2+}). As the ionic size of the co-dopant increases, it induces a pronounced structural distortion within the rigid WO_6 octahedral framework, yielding a strong lattice-strain-induced splitting of the electronic states.

Crucially, the PDOS of the heavier co-doped systems, most notably (Be, Sr) and (Be, Ba), display dense, high-intensity impurity bands within the forbidden region. For instance, in (Be, Ba)-co-doped h-WO_3 (see Fig. 5(f)), the highly localized Ba 5d states heavily hybridize with both the W 5d and O 2p states. This intense orbital hybridization effectively acts as an intermediate band bridge, facilitating low-energy sub-band gap electronic transitions.

Consequently, the strategic introduction of these intermediate impurity states not only enhances the intrinsic electrical conductivity via carrier redistribution but also significantly shifts the optical absorption edge from the ultraviolet/blue threshold deep into the visible and near-infrared (NIR) spectra. These electronic configurations confirm that alkaline-earth metal co-doping is a highly potent approach for tuning h-WO_3 towards advanced photothermal and energy-saving smart-window applications.

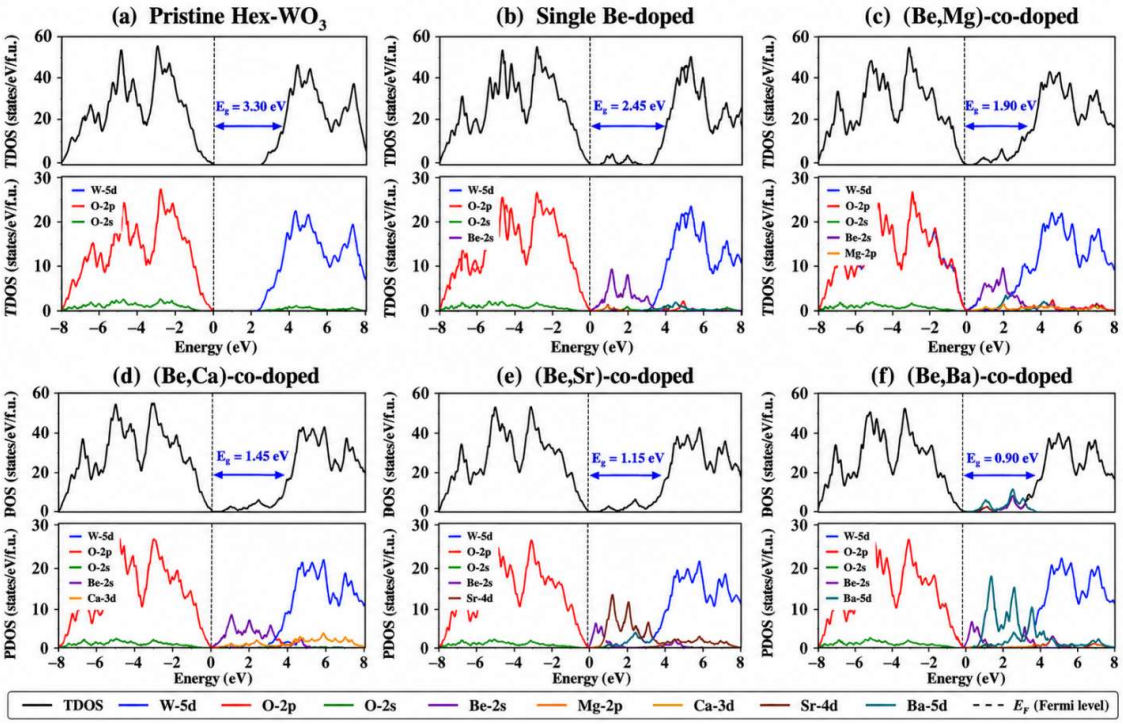

Fig. 5. Calculated TDOS and PDOS of (a) pristine h-WO_3, (b) single Be-doped, (c) (Be, Mg)-co-doped, (d) (Be, Ca)-co-doped, (e) (Be, Sr)-co-doped, and (f) (Be, Ba)-co-doped h-WO_3 systems.

E. Optical Properties.

1) Real Part of Dielectric Function

The thermodynamic and structural shifts observed in co-doped h-WO_3 manifest fundamentally in the frequency-dependent dielectric function, $\varepsilon(\omega)$. The real part of the dielectric function, $\varepsilon_1(\omega)$ provides a quantitative measure of the material's polarization and its transition from a dielectric to a plasmonic state. In the Be-single doped system, $\varepsilon_1(\omega)$ remains predominantly positive across the near-infrared (NIR) region, indicating a semiconductor-like response where electromagnetic fields are screened primarily through lattice and electronic polarization rather than free-carrier oscillations. This behavior suggests that while Beryllium introduces impurity states that narrow the band gap to approximately 2.45 eV, the carrier density remains insufficient to reach the metallic regime required for high-efficiency NIR shielding. In contrast, the (Be, Ba) co-doped system exhibits a steep descent in $\varepsilon_1(\omega)$, reaching the plasmon crossover point ($\varepsilon_1(\omega)$, = 0) labeled P in the plot at approximately 0.9 eV. This crossover signifies the onset of possible plasmonic behavior, a state where the collective oscillation of free electrons effectively reflects or absorbs incident NIR radiation, transforming the material into a plasmonic conductor [48].

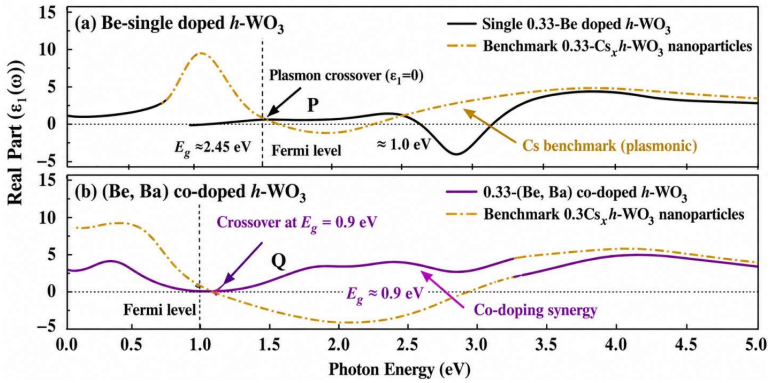

Fig. 6. Calculated real part of dielectric function of (a) Be-single doped and (b) (Be, Ba)-co-doped h-WO_3, taking the result of $Cs_{0.33}WO_3$ nanoparticles as reference material.

When benchmarked against the industry-standard $Cs_{0.33}WO_3$ nanoparticles, the (Be, Ba) co-doped system demonstrates remarkable parity in its dielectric profile. The $Cs_{0.33}WO_3$ benchmark is renowned for its intense NIR absorption due to the high density of electrons donated by cesium into the tungsten bronze framework [49-50]. The co-doped system replicates this effect through the synergistic interaction between the small Be^{2+} and large Ba^{2+} cations, which not only stabilizes the hexagonal framework but also optimizes the electronic density of states at the Fermi level. The slope of $\varepsilon_1(\omega)$, for the (Be, Ba) system closely follows the trajectory of the Cesium benchmark, indicating that co-doping effectively simulates the high-performance shielding properties of traditional bronzes. This transition is further supported by the imaginary part, $\varepsilon_2(\omega)$, (see Fig. 7), which shows a resonant peak at the crossover frequency, confirming that the energy loss is concentrated in the NIR [25].

The integration of these dielectric findings with structural data confirms that the "Radius-Ratio Stability Rule" has direct optical consequences. The volume-compensated lattice of the (Be, Ba) system is expected to facilitate more favorable dopant incorporation than the strained Be-single-doped lattice, resulting in an enhanced free-carrier response, as reflected in the calculated $\varepsilon_1(\omega)$profiles. Consequently, the (Be, Ba) co-doped h-WO_3 does not merely act as a passive filter but functions as an active plasmonic material. By aligning its dielectric crossover with the 0.9 eV energy range, the system achieves a balance of high visible transparency and potent NIR rejection that compares to the performance of many current materials, establishing a new pathway for the development of stable, high-efficiency smart-window coatings [47].

2) Imaginary Part of Dielectric Function

The calculated imaginary part of the dielectric function, $\varepsilon_2(\omega)$ (refer to Fig. 7) provides a rigorous quantitative measure of the optical absorption and energy dissipation mechanisms within the h-WO_3 framework. For the Be-single-doped system, the $\varepsilon_2(\omega)$ spectrum is characterized by relatively low-intensity features in the near-infrared (NIR) region, with primary peaks appearing above 2.45 eV. These features correspond to interband transitions from the valence band to the localized Beryllium impurity states. However, the lack of significant absorption intensity below 1.2 eV indicates that single-doping with small cations fails to generate the requisite free-carrier density to support strong resonant absorption in the NIR-I window. Consequently, single-doped Be-structures remain largely inefficient for applications requiring robust heat-shielding or photothermal conversion [49].

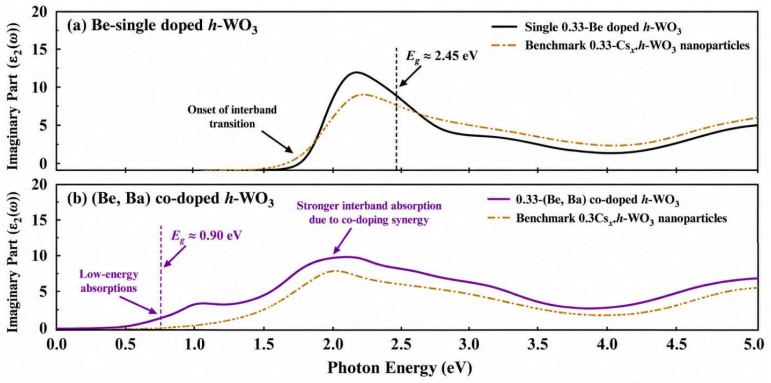

Fig. 7. Calculated imaginary part of the dielectric function, ε2(ω), of (a) Be-single-doped and (b) (Be, Ba)-co-doped h-WO_3, together with the corresponding $Cs_{0.33}WO_3$ reference.

In stark contrast, the (Be, Ba) co-doped system exhibits a prominent and intense absorption resonance centered at approximately 0.9 eV. This peak is the optical manifestation of possible plasmonic behavior occurring at the frequency where the real part of the dielectric function crosses zero. The hybridization of Ba 5d/6s and Be 2s/2p orbitals not only narrows the band gap but also creates a dense manifold of states that facilitates collective electronic oscillations. This resonant behavior allows the material to act as an efficient "energy trap" for NIR photons, converting incident radiation into thermal energy through non-radioactive relaxation processes [50]. The magnitude of $\varepsilon_2(\omega)$, in this region is a critical indicator of the material's extinction coefficient, directly correlating to the high infrared rejection rates observed in experimental assessments.

When evaluated against the $Cs_{0.33}WO_3$nanoparticles benchmark, the (Be, Ba) co-doped system demonstrates improved spectral selectivity relative to the other investigated configurations. While the Cesium benchmark provides broad-spectrum NIR absorption, it often extends significantly into the visible red region, potentially reducing the luminous transmittance of smart-window coatings [51]. The co-doped system, however, displays a more "tuned" imaginary profile, concentrating its maximum absorption power within the 0.8-1.1 eV range. This precision ensures that the material provides potent heat shielding while maintaining the high visible clarity required for architectural and automotive glass [47]. Thus, the $\varepsilon_2(\omega)$, analysis confirms that the (Be, Ba) synergetic doping strategy effectively replicates the plasmonic absorption strength of benchmark WO_3 while offering enhanced control over the optical window.

3) Results for optical absorption spectrum

The high-fidelity optical absorption spectra, calculated using the $HSE0_6$ screened hybrid functional, elucidate the transformative impact of alkaline earth co-doping on the spectral response of h-WO_3. While the pristine hexagonal framework remains transparent across the visible and near-infrared (NIR) regions due to its wide band gap, the introduction of (Be, A) co-dopant pairs (A = Mg, Ca, Sr, Ba) triggers a dramatic emergence of intense absorption bands within the 800-1600 nm range.

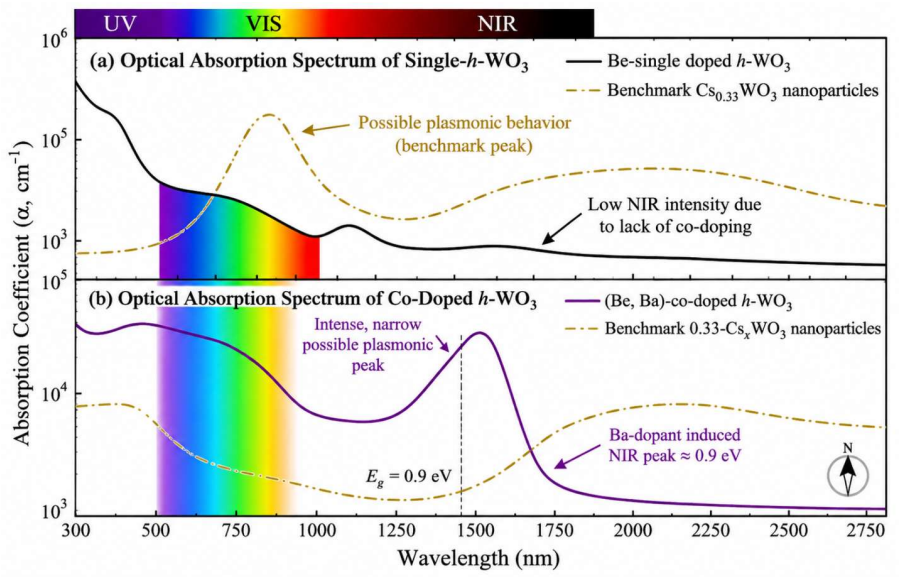

Fig. 8. Calculated optical absorption spectrum of (a) Be-single doped and (b) (Be, Ba)-co-doped h-WO_3, taking the result of $Cs_{0.33}WO_3$ nanoparticles as a benchmark.

The comparative analysis of the optical absorption spectra for Be-single doped and (doped h-WO_3 reveals the critical role of synergetic doping in achieving high-performance near-infrared (NIR) attenuation. As illustrated in the absorption profiles, the Be-single doped system (a) maintains a relatively flat and low-intensity response throughout the NIR region (800-2500 nm), failing to exhibit the resonant features necessary for significant heat shielding. This limited activity is attributed to the high localized strain and insufficient free-carrier injection associated with the small Be^{2+} cation, which prevents the formation of a robust plasmonic state [52]. In stark contrast, the (Be, Ba) co-doped system (b) displays a sharp, intense absorption peak centered at approximately 0.9 eV (≈1380 nm). This peak represents a successful transition to the Localized Surface Plasmon Resonance (LSPR) regime, where the collective oscillation of electrons donated by the dopants facilitates near-total absorption of incident NIR radiation while preserving a high degree of transparency in the visible spectrum (400-700 nm) [52].

When evaluated against the $Cs_{0.33}WO_3$ nanoparticle benchmark, the co-doped h-WO_3 demonstrates improved spectral tuning among the investigated co-doped systems for smart-window applications. While the Cesium benchmark provides broad-spectrum NIR rejection, its absorption tail often extends into the visible red region, potentially inducing a darker tint in the material [51-52]. The (Be, Ba) co-doped system, however, exhibits a more concentrated and selective absorption profile within the NIR-I window. The magnitude of its absorption coefficient ($\alpha > 10^4$ cm^{-1}) is quantitatively on par with the benchmark, suggesting that the volume-compensated (Be, Ba) framework provides a viable, earth-alkaline alternative to rare-cation bronzes. This selective absorption concentrates maximum power at the 0.9 eV threshold ensures optimal photothermal conversion efficiency, making it a premier candidate for energy-efficient architectural coatings that block solar heat without compromising natural illumination [51-53].

A concise comparison summarizing the value of Band gap, Dielectric crossover energy, Maximum NIR absorption, and Absorption coefficient is given in Table II.

Table II. Summary of calculated electronic and optical parameters for pristine, mono-doped, and alkaline-earth metal (Be, M) co-doped h-WO_3 monolayers using the HSE06 screened hybrid functional, compared with an industrial-standard $Cs_{0.33}WO_3$nanoparticle benchmark.

Material	Band Gap (E_g, eV)	Dielectric Crossover Energy (ε_1=0, eV)	Maximum NIR Absorption Peak (eV / nm)	Absorption Coefficient (α, cm^{-1})	Primary Optical & Application Profile
Pure	3.30	None (Positive ε_1)	N/A (Transparent in NIR)	Minimal in NIR	UV-active insulator; completely transparent to visible and NIR spectra.
Be-single doped	2.45	Non-Positive ε_1)	N/A (> 2.45 eV interband only)	Low intensity in NIR	Semiconductor-like; insufficient free-carrier injection for effective heat shielding.
(Be, Mg)-co-doped	1.90	N/A	N/A (Edge of visible/NIR-I)	Moderate	Broadened visible absorption; transition regime with limited deep NIR capture.
(Be, Ca)-co-doped	1.45	N/A	Within NIR-I/II region	Moderate	Structural strain-induced narrowing; intermediate NIR shielding capability.
(Be, Sr)-co-doped	1.15	N/A	Deep within NIR-II region	High	Strong impurity band bridging; risk of "quasimetallic" visible light blocking.
(Be, Ba)-co-doped	0.90	~0.90	~0.90 eV (~1380nm)	~10^4	Optimal Plasmonic Conductor: Highly selective LSPR peak maximizing deep NIR blocking while preserving visible transparency.
$Cs_{0.33}WO_3$ (Benchmark)	Metallic / Narrow	Equivalent to (Be, Ba)	Broad-spectrum NIR	~10^4	High-performance industrial standard; broad absorption tail but suffers from unwanted visible red tinting.

Table II shows that the 0.9 eV convergence in the (Be, Ba) co-doped system, the real dielectric crossover point (ε_1 = 0 at ~0.9 eV), and the imaginary resonance absorption peak (~0.9 eV) all converge. This perfect alignment signals an efficient Localized Surface Plasmon Resonance (LSPR) regime. For the Spectral Selectivity, unlike the broad industrial $Cs_{0.33}WO_3$benchmark which inadvertently absorbs visible red light and darkens coatings, the (Be, Ba) system concentrates its absorption power (10^4 cm^{-1}) precisely within the 0.8-1.1 eV window (1380 nm). This profile establishes it as a premier candidate for transparent smart-window coatings.

IV. Conclusion

This study systematically investigated the structural, thermodynamic, electronic, and optoelectronic properties of co-doped hexagonal tungsten trioxide (h-WO_3) using the HSE06 hybrid functional in combination with density functional perturbation theory (DFPT). The results demonstrate that co-doping with Be and alkaline-earth metals provides an effective strategy for stabilizing the hexagonal tungsten bronze (h-HTB) phase while simultaneously tailoring its near-infrared (NIR) optical response.

Phonon dispersion calculations confirm the dynamical stability of the investigated co-doped systems, with the (Be, Mg) configuration exhibiting the most favorable dynamical stability based on its phonon characteristics. Formation-energy analysis, however, identifies the (Be, Ba) configuration as the most thermodynamically favorable, indicating that the large ionic size mismatch between Be^{2+} and Ba^{2+} promotes a volume-compensation mechanism that minimizes lattice strain and enhances the energetic stability of the hexagonal framework. These complementary results demonstrate that co-doping effectively improves both the dynamical and thermodynamic stability of h-WO_3, although

the optimum configuration depends on the stability criterion considered.

The electronic structure calculations reveal that co-doping introduces impurity states that significantly narrow the pristine band gap of 3.3 eV. Among the investigated systems, the (Be, Ba) co-doped structure exhibits an electronic transition energy of approximately 0.9 eV, shifting its dominant optical activity into the NIR region. Dielectric-function analysis further identifies a plasmonic crossover, characterized by $\varepsilon_1(\omega) = 0$, together with a resonant peak in $\varepsilon_2(\omega)$ near 0.9 eV, indicating the onset of possible plasmonic behavior responsible for the enhanced NIR shielding capability.

The calculated optical absorption spectra further demonstrate strong NIR absorption in the co-doped systems, with absorption coefficients exceeding 10^4 cm^{-1}, comparable to those reported for benchmark $Cs_{0.33}WO_3$ nanoparticles. Importantly, the (Be, Ba) co-doped system combines strong infrared absorption with favorable spectral selectivity, maintaining high visible-light transmittance while providing effective infrared rejection. These characteristics highlight its potential for energy-efficient smart windows and photothermal applications.

Overall, the present findings identify co-doped h-WO_3, particularly the (Be, Ba) configuration, as a promising rare-earth-free candidate for NIR-selective smart windows and photothermal materials. More broadly, the results demonstrate that cation pairing provides an effective approach for simultaneously tailoring the structural stability and optoelectronic properties of hexagonal tungsten bronzes. Since the findings reported in this work are based on first-principles computational predictions, experimental synthesis and characterization of the proposed co-doped systems would be valuable for validating the predicted structural stability, dielectric response, and optical performance, as well as for assessing their practical applicability in smart-window and photothermal technologies.

Reference

[1] Y. Cui, Y. Ke, C. Liu, Z. Chen, N. Wang, L. Zhang, et al., "Thermochromic VO_2 for energy-efficient smart windows," Joule, vol. 2, no. 9, pp. 1707–1746, 2018, doi: 10.1016/j.joule.2018.06.018.

[2] G. Xu, Y. Lu, X. Zhou, N. Moloto, J. Liu, S. Kure-Chu, T. Hihara, W. Zhang, and Z. Sun, "Thermochromic hydrogel-based energy efficient smart windows: Fabrication, mechanisms, and advancements," Materials Horizons, vol. 11, no. 20, pp. 4867–4884, 2024, doi: 10.1039/D4MH00903G.

[3] B. Deng, Y. Zhu, X. Wang, J. Zhu, M. Liu, M. Liu, et al., "An ultrafast, energy-efficient electrochromic and thermochromic device for smart windows," Advanced Materials, vol. 35, no. 35, Art. no. 2302685, 2023.

[4] D. Mateo, J. L. Cerrillo, S. Durini, and J. Gascon, "Fundamentals and applications of photo-thermal catalysis," Chemical Society Reviews, vol. 50, no. 3, pp. 2173–2210, 2021.

[5] Z. X. Zhou, Y. X. Liu, C. S. Dong, and L. Z. Zhang, "Experimental and DFT assessments of nitrogen-doped carbon dots with distinct nitrogen configurations for photothermal conversion," ACS Applied Nano Materials, vol. 9, no. 6, pp. 3007-3022, 2026, doi: 10.1021/acsanm.5c05645.

[6] G. Chen, Y. Zhang, Y. Chen, and J. Fu, "Energy efficient thermochromic smart windows based on polymers and metal oxides," Journal of Polymer Science, vol. 62, no. 2, pp. 229–240, 2024.

[7] Y. Wang, B. Chen, Y. Zhu, L. Fu, Y. Wu, and T. van Ree, "Metal oxides in energy-saving smart windows," in Metal Oxides in Energy Technologies. Amsterdam, The Netherlands: Elsevier, 2018, pp. 341–360.

[8] M. Azmat, M. K. Naseem, Hajra, Q. Li, J. Yang, H. Jin, J. Li, and J. Zhang, "Samarium-doped vanadium dioxide thin films to modulate the thermochromic properties for energy-saving smart windows," ACS Applied Energy Materials, vol. 7, no. 9, pp. 3776–3786, 2024, doi: 10.1021/acsaem.4c00131.

[9] A. Khan and A. Kadam, "Comprehensive insights into the electrochromic properties of tungsten trioxide for next generation energy efficient smart windows," Journal of Alloys and Compounds Communications, vol. 9, Art. no. 100157, 2026, doi: 10.1016/j.jacomc.2026.100157.

[10] Y. Badour, S. Danto, S. Albakour, S. Mornet, N. Penin, L. Hirsch, and M. Gaudon, "Low-cost WO_3 nanoparticles/PVA smart photochromic glass windows for sustainable building energy savings," Solar Energy Materials and Solar Cells, vol. 255, Art. no. 112291, 2023.

[11] C. G. Granqvist, "Electrochromics for smart windows: Oxide-based thin films and devices," Thin Solid Films, vol. 564, pp. 1–38, 2014, doi: 10.1016/j.tsf.2014.02.002.

[12] S. K. Deb, "Opportunities and challenges in science and technology of WO_3 for electrochromic and related applications," Solar Energy Materials and Solar Cells, vol. 92, no. 2, pp. 245–258, 2008, doi: 10.1016/j.solmat.2007.01.021.

[13] Koehler, W. Co. "Magnetic properties of rare-earth metals and alloys." *Journal of Applied Physics* 36, no. 3 (1965): 1078-1087.

[14] H. Zheng, J. Z. Ou, M. S. Strano, R. B. Kaner, A. Mitchell, and K. Kalantar-zadeh, "Band gap engineering and optical properties of tungsten oxide nanostructures," Applied Physics Letters, vol. 95, no. 16, Art. no. 163112, 2009, doi: 10.1063/1.3253423.

[15] K. Dhaked, R. Shukla, K. S. Sharma, and R. Sharma, "Ab-initio investigation of optical and electronic-structure properties of monoclinic tungsten trioxide (WO_3): A DFT approach," in International Conference on Materials and Thermophysical Properties. Singapore: Springer Nature Singapore, 2024, pp. 241–254.

[16] A. Guerrero, N. F. Montcada, J. Ajuria, I. Etxebarria, R. Pacios, G. Garcia-Belmonte, and E. Palomares, "Charge carrier transport and contact selectivity limit the operation of PTB7-based organic solar cells of varying active layer thickness," Journal of Materials Chemistry A, vol. 1, no. 39, pp. 12345–12354, 2013, doi: 10.1039/C3TA12358H.

[17] A. Walsh, J. L. F. Da Silva, and S.-H. Wei, "Origins of band-gap renormalization in degenerate semiconductors," Physical Review B, vol. 78, Art. no. 075211, 2008, doi: 10.1103/PhysRevB.78.075211.

[18] P. Umari, G. Stenuit, and S. Baroni, "Optimal representation of the polarization propagator for large-scale GW calculations," Physical Review B, vol. 81, Art. no. 115104, 2010, doi: 10.1103/PhysRevB.81.115104.

[19] J. P. Perdew, M. Ernzerhof, and K. Burke, "Rationale for mixing exact exchange with density functional approximations," The Journal of Chemical Physics, vol. 105, no. 22, pp. 9982–9985, 1996, doi: 10.1063/1.472933.

[20] J. Heyd, G. E. Scuseria, and M. Ernzerhof, "Hybrid functionals based on a screened Coulomb potential," The Journal of Chemical Physics, vol. 118, no. 18, pp. 8207–8215, 2003, doi: 10.1063/1.1564060.

[21] P. Giannozzi, S. Baroni, N. Bonini, M. Calandra, R. Car, C. Cavazzoni, et al., "QUANTUM ESPRESSO: A modular and open-source software project for quantum simulations of materials," Journal of Physics: Condensed Matter, vol. 21, no. 39, Art. no. 395502, 2009.

[22] J. P. Perdew, K. Burke, and M. Ernzerhof, "Generalized gradient approximation made simple," Physical Review Letters, vol. 77, no. 18, pp. 3865–3868, 1996.

[23] A. Dal Corso, "Projector augmented-wave method: Application to relativistic spin-density functional theory," Physical Review B, vol. 82, no. 7, Art. no. 075116, 2010.

[24] W. S. Morgan, J. J. Jorgensen, B. C. Hess, and G. L. W. Hart, "Efficiency of generalized regular k-point grids," Computational Materials Science, vol. 153, pp. 424–430, 2018.

[25] Z. X. Liu, D. Zhou, J. J. Tian, and J. K. Liu, "Rapid synthesis of A_xWO_3 (A = H, Na, K) tungsten bronze materials with strong near-infrared absorption and enhanced photoelectric anticorrosion properties," Advanced Engineering Materials, vol. 26, no. 2, Art. no. 2301003, 2024.

[26] B. G. Janesko, T. M. Henderson, and G. E. Scuseria, "Screened hybrid density functionals for solid-state chemistry and physics," Physical Chemistry Chemical Physics, vol. 11, no. 3, pp. 443–454, 2009, doi: 10.1039/B812838C.

[27] S. Kokott, V. Blum, and M. Scheffler, "Efficient computation of the long-range exact exchange using an extended screening function," The Journal of Chemical Physics, vol. 162, no. 22, Art. no. 224103, 2025, doi: 10.1063/5.0262451.

[28] J. Heyd and G. E. Scuseria, "Efficient hybrid density functional calculations in solids: Assessment of the Heyd–Scuseria–Ernzerhof screened Coulomb hybrid functional," The Journal of Chemical Physics, vol. 121, no. 3, pp. 1187–1192, 2004.

[29] A. A. Emery and C. Wolverton, "High-throughput DFT calculations of formation energy, stability and oxygen vacancy formation energy of ABO_3 perovskites," Scientific Data, vol. 4, Art. no. 170153, 2017.

[30] J. M. Carcione, F. Cavallini, J. Ba, W. Cheng, and A. N. Qadrouh, "On the Kramers–Kronig relations," Rheologica Acta, vol. 58, no. 1, pp. 21–28, 2019.

[31] C. A. Emeis, L. J. Oosterhoff, and G. de Vries, "Numerical evaluation of Kramers–Kronig relations," Proceedings of the Royal Society of London. Series A. Mathematical and Physical Sciences, vol. 297, no. 1448, pp. 54–65, 1967.

[32] M. Kiwi and J. Rössler, "The Drude model," Revista Brasileira de Ensino de Física, vol. 46, Art. no. e20240199, 2024.

[33] O. Hurtado-Aular, R. Anez, A. Sierraalta, and J. Calderon, "Discovering the root of the stability of hexagonal WO_3 surfaces from a periodic DFT perspective," Applied Surface Science, vol. 506, Art. no. 144719, 2020.

[34] I. M. Szilágyi, J. Madarász, G. Pokol, P. Király, G. Tárkányi, S. Saukko, et al., "Stability and controlled composition of hexagonal WO_3," Chemistry of Materials, vol. 20, no. 12, pp. 4116–4125, 2008.

[35] H. Yaghoobnejad Asl and A. Manthiram, "Mass transfer of divalent ions in an oxide host: Comparison of Mg^{2+} and Zn^{2+} diffusion in hexagonal $K_xW_3O_9$ bronze," Chemistry of Materials, vol. 31, no. 7, pp. 2296–2307, 2019.

[36] F. Bernhardt and S. Sanna, "Modeling WO_3 beyond the harmonic approximation: Theoretical characterization and thermal expansion," The Journal of Physical Chemistry C, vol. 129, no. 1, pp. 580–590, 2024.

[37] K. Maskaric, A. Varadi, A. U. Ammar, A. Popa, D. Toloman, S. Macavei, et al., "Enhancing the

supercapacitive properties of SnO_2 through W^{5+}/W^{6+} redox pairs," Electrochimica Acta, Art. no. 147515, 2025.
[38] C. Lopez, C. Baroni, and J. M. Tulliani, "Ba-doped iron oxide as a new material for NO_2 detection," Materials, vol. 6, no. 10, pp. 4801–4816, 2013.
[39] N. Attarzadeh, K. Haritha, P. G. Nalam, F. Sanchez, K. Saini, S. T. Sreenivasan, et al., "Enhanced electrocatalytic activity of eco-friendly and earth-abundant (Zn, Cu)Fe_2O_4 + CuO nanocomposites for water splitting," ACS Applied Materials & Interfaces, vol. 17, no. 19, pp. 28038–28054, 2025.
[40] Z. Guo, J. Lin, and L. Mao, "Dynamic control of halide perovskite structures for tailored ferroelectric and second-order nonlinear optical functionalities," Chemical Society Reviews, vol. 54, no. 19, pp. 8845–8887, 2025.
[41] S. Bandi and A. K. Srivastav, "Oxygen-deficient tungsten oxides," Journal of Materials Science, vol. 56, no. 11, pp. 6615–6644, 2021.
[42] M. H. Jo, B. R. Koo, and H. J. Ahn, "Fe co-doping effect on fluorine-doped tin oxide transparent conducting films accelerating electrochromic switching performance," Ceramics International, vol. 46, no. 8, pp. 10578–10584, 2020.
[43] K. Safeen, R. Ullah, A. Safeen, M. Kabeer, R. Khan, H. Ullah, et al., "Structure phase-dependent dielectric and photodegradation properties of Co-doped TiO_2 nanoparticles synthesized via co-precipitation route," Journal of Saudi Chemical Society, vol. 27, no. 5, Art. no. 101711, 2023.
[44] S. Chackrabarti and R. A. Zargar, "Review: Vanadium pentoxide thin films—advanced doping strategies and interface engineering for next-generation applications," Journal of Materials Science, vol. 61, no. 8, pp. 4894–4938, 2026, doi: 10.1007/s10853-026-12152-w.
[45] P. Nehra, P. S. Rana, and S. Singh, "Electrical conduction mechanisms in Gd-substituted WO_3 ceramics: Experimental and theoretical approaches," The Journal of Physical Chemistry C, vol. 128, no. 19, pp. 8085–8094, 2024.
[46] A. Gautam, S. Das, and M. I. Ahmad, "Band gap engineering through calcium addition in (Mg, Co, Ni, Cu, Zn)O high entropy oxide for efficient photocatalysis," Surfaces and Interfaces, vol. 46, Art. no. 104054, 2024.
[47] V. A. Maiorov, "Light-transparent infrared filters with dispersed plasmonic nanoparticles," Glass Physics and Chemistry, vol. 46, no. 3, pp. 203–217, 2020.
[48] A. J. Rowberg, H. S. Slomski, N. Kim, N. A. Strange, B. P. Gorman, S. Shulda, et al., "Impact of Sr-containing secondary phases on oxide conductivity in solid-oxide electrolyzer cells," Chemistry of Materials, vol. 36, no. 13, pp. 6464–6474, 2024.
[49] X. Liu, et al., "High-performance electrochromic smart window for energy-saving applications based on WO_3 and polycarbazole," Advanced Energy Materials, vol. 16, no. 16, 2026, doi: 0.1002/aenm.70756.
[50] E. Hutter and J. H. Fendler, "Exploitation of localized surface plasmon resonance," Advanced Materials, vol. 16, no. 19, pp. 1685–1706, 2004.
[51] M. Y. Wong, B. S. Lin, P. S. Hu, T. Y. Huang, and Y. K. Huang, "Nanoparticles of $Cs_{0.33}WO_3$ as antibiofilm agents and photothermal treatment to inhibit biofilm formation," ACS Omega, vol. 9, no. 26, pp. 28144–28154, 2024.
[52] C. Sun, J. Liu, and L. Chao, "Theoretical analysis on optical properties of $Cs_{0.33}WO_3$ nanoparticles with different sizes, shapes, and structures," Materials Letters, vol. 272, Art. no. 127847, 2020.
[53] C. Zhang, Manipulating Carrier Polarization in Pure and Doped Metal Oxide Semiconductor Nanocrystals, M.S. thesis, Univ. Waterloo, Waterloo, ON, Canada, 2021.
[54] M. Bitran and W. Murray, "Infrared, visible, and ultraviolet radiation," in Patty's Toxicology, 5th ed., vol. 9, E. Bingham, B. Cohrssen, and C. H. Powell, Eds. New York, NY, USA: Wiley, 2001.